Experimental evaluation of x-ray acoustic computed tomography for radiotherapy dosimetry applications

Susannah Hickling[a)]
Department of Physics and Medical Physics Unit, McGill University, Cedars Cancer Centre, Montreal, QC, Canada H4A 3J1

Hao Lei
Department of Mechanical Engineering, University of Michigan, Ann Arbor, MI 48109, USA

Maritza Hobson and Pierre Léger
Medical Physics Unit, McGill University Health Centre, Cedars Cancer Centre, Montreal, QC H4A 3J1, Canada

Xueding Wang
Departments of Radiology and Biomedical Engineering, University of Michigan, Ann Arbor, MI 48109-0600, USA

Issam El Naqa
Department of Radiation Oncology, University of Michigan, Ann Arbor, MI 48103-4943, USA

(Received 10 May 2016; revised 25 November 2016; accepted for publication 29 November 2016; published 25 January 2017)

Purpose: The aim of this work was to experimentally demonstrate the feasibility of x-ray acoustic computed tomography (XACT) as a dosimetry tool in a clinical radiotherapy environment.
Methods: The acoustic waves induced following a single pulse of linear accelerator irradiation in a water tank were detected with an immersion ultrasound transducer. By rotating the collimator and keeping the transducer stationary, acoustic signals at varying angles surrounding the field were detected and reconstructed to form an XACT image. Simulated XACT images were obtained using a previously developed simulation workflow. Profiles extracted from experimental and simulated XACT images were compared to profiles measured with an ion chamber. A variety of radiation field sizes and shapes were investigated.
Results: XACT images resembling the geometry of the delivered radiation field were obtained for fields ranging from simple squares to more complex shapes. When comparing profiles extracted from simulated and experimental XACT images of a 4 cm × 4 cm field, 97% of points were found to pass a 3%/3 mm gamma test. Agreement between simulated and experimental XACT images worsened when comparing fields with fine details. Profiles extracted from experimental XACT images were compared to profiles obtained through clinical ion chamber measurements, confirming that the intensity of XACT images is related to deposited radiation dose. Seventy-seven percent of the points in a profile extracted from an experimental XACT image of a 4 cm × 4 cm field passed a 7%/4 mm gamma test when compared to an ion chamber measured profile. In a complicated puzzle-piece shaped field, 86% of the points in an XACT extracted profile passed a 7%/4 mm gamma test.
Conclusions: XACT images with intensity related to the spatial distribution of deposited dose in a water tank were formed for a variety of field sizes and shapes. XACT has the potential to be a useful tool for absolute, relative and *in vivo* dosimetry. © *2016 American Association of Physicists in Medicine* [https://doi.org/10.1002/mp.12039]

Key words: radiation dosimetry, thermoacoustics, ultrasonics, X-ray acoustic computed tomography

1. INTRODUCTION

Radiation dosimetry is a crucial process in radiation therapy (RT) to ensure that the correct dose is accurately delivered to the desired location.[1,2] *Ex vivo* dosimetry, whether it be absolute or relative, refers to the measurement of radiation dose in a representative phantom, and is important for beam calibration, treatment planning, and quality assurance purposes. *In vivo* dosimetry is the measurement of radiation dose received by a patient during treatment. The International Atomic Energy Agency (IAEA) recommends that *in vivo* dosimetry be performed in patients undergoing new treatment techniques, after changes to software/equipment, single fraction treatments, and treatments with a curative intent where the dose received is potentially close to normal tissue tolerance.[3] Due to the increase in more advanced treatment delivery techniques, such as intensity modulated RT (IMRT) and volumetric arc therapy (VMAT), and stereotactic cases with single or hypofractionated deliveries, the demand and necessity for accurate and real-time *in vivo* dosimetry is likely to be on the rise.

A wide variety of techniques are currently used for clinical dosimetry. The most established of these include ion chambers (ICs), diodes, thermoluminescent dosimeters (TLDs), optically stimulated luminescent dosimeters (OSLDs), metal oxide semiconductor field effect transistors (MOSFETs),

electronic portal imaging devices (EPIDs), and film.[4] All of these techniques have limitations, whether it be they only give point measurements, are not real-time, are dose rate or energy dependent, or are not economical.

The photoacoustic effect is a physical phenomenon discovered by Alexander Graham Bell whereby acoustic waves are induced following the absorption of heat energy from a pulsed photon beam.[5] The rapid deposition of heat energy within a material leads to a localized temperature increase, causing thermoelastic expansion and the induction of a differential pressure distribution. This leads to the generation of acoustic waves that propagate throughout the medium. The properties of these acoustic waves are dependent on a number of factors, including the amount of heat energy deposited, the shape of the heat energy distribution, and the material properties of the sample.[6] By detecting the acoustic waves at various angles surrounding the irradiated sample with a pressure sensor such as an ultrasound transducer or hydrophone, an image of the initial differential pressure distribution can be reconstructed. The photoacoustic effect has been exploited by photoacoustic imaging to form images with contrast based on optical photon absorption.[7,8]

The generation of acoustic waves via the photoacoustic effect following x-ray irradiation was first demonstrated using x-rays produced by a high-energy synchrotron source.[9] Bowen et al. showed the first experimental detection of acoustic waves induced following irradiation by a clinical radiotherapy linear accelerator (linac) photon beam.[10] More recently, Xiang et al. proposed x-ray acoustic computed tomography (XACT), the x-ray equivalent of optical laser photoacoustic imaging.[11] They showed a preliminary demonstration of XACT by imaging a lead rod embedded in chicken breast tissue. XACT using pulsed x-ray tubes in the keV energy range has also been recently proposed as a novel imaging modality, and a resolution of 350 μm has been achieved using a 60 ns x-ray pulse.[12]

Since contrast in XACT arises from a material's differing x-ray absorption properties, it has long been proposed that detecting the acoustic waves induced following linac irradiation has potential applications in radiotherapy dosimetry.[10,11,13] Recent research in this area has focused on the development of a comprehensive simulation workflow and experimental measurements to systematically evaluate the properties of linac irradiation induced acoustic waves,[13] the use of hydrophones to detect the induced acoustic signals in an effort to improve signal to noise ratio (SNR),[14] and demonstrating the ability to image lead samples using a commercial ultrasound scanner.[15]

Previous work on XACT has largely concentrated on investigating the acoustic signals induced following the irradiation of high-density materials, such as lead blocks, presumably due to the relatively large induced acoustic signal. This work demonstrates the ability to form experimental XACT images in pure water in a variety of clinically relevant situations and to extract accurate dosimetric information from such images. The characteristics of the induced acoustic waves and resulting XACT images are investigated. In addition, experimental and simulated XACT images are compared, and XACT is demonstrated to be a viable dosimetry technique by comparing profiles extracted from experimental XACT images to clinical ion chamber measurements.

2. MATERIALS AND METHODS

2.A. XACT experimental setup

Experimental XACT images were acquired by irradiating a water tank using a clinical radiotherapy linac. A 10 MV flattening filter free (FFF) photon beam produced by a TrueBeam™ (Varian Medical Systems, Palo Alto, CA, USA) linac was used for irradiation. The linac was operated at a dose rate of 800 MU/min. Under these conditions, the linac runs at a pulse repetition frequency of 120 Hz and is calibrated to deliver 1.11 mGy per pulse at 2.4 cm, the depth of maximum dose. This corresponds to a per pulse temperature increase of 264 nK at the depth of maximum dose. Figure 1 displays the linac pulse shape, which was found to have a full width at half maximum (FWHM) length of 4 μs, as determined through measuring the linac target pulse with an oscilloscope. Note that this pulse represents the pulse envelope formed by the series of high frequency picosecond pulses produced by the microwave generator.

As illustrated in Fig. 2, the water tank sat on the linac couch at a source to surface distance (SSD) of 100 cm. An unfocused, circular immersion ultrasound transducer with a central frequency of 0.5 MHz, a diameter of 25.4 mm, and a – 6 dB bandwidth of 64% (V301-SU, Olympus-NDT, Waltham, MA, USA) was used to detect the induced acoustic waves. The transducer was placed 13.7 cm away from the center of the radiation field at the desired imaging depth, and oriented perpendicularly to the central axis of the linac photon beam. The output of the transducer was fed into a commercial preamplifier (5660B, Olympus- NDT, Waltham, MA, USA) set to a gain of 60 dB with a −3 dB bandwidth of 20 kHz–2 MHz. Signals were read out on an oscilloscope (InfiniVision, DSO-X 2012A, Agilent Technologies, Santa Clara, CA, USA) situated at the treatment console. The linac

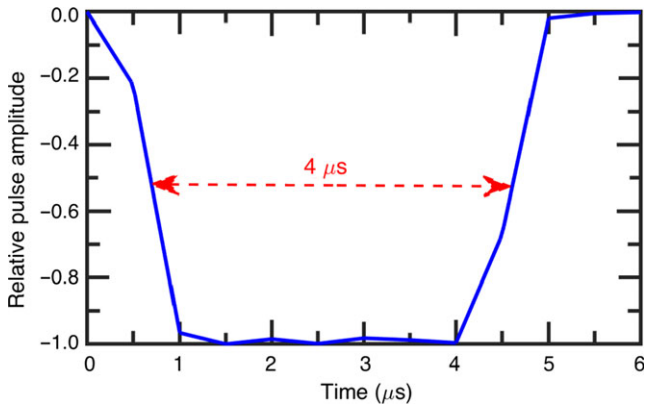

FIG. 1. Linac target pulse produced by a Varian TrueBeam accelerator for a 10 MV FFF beam. The pulse has a FWHM length of 4 μs. [Color figure can be viewed at wileyonlinelibrary.com]

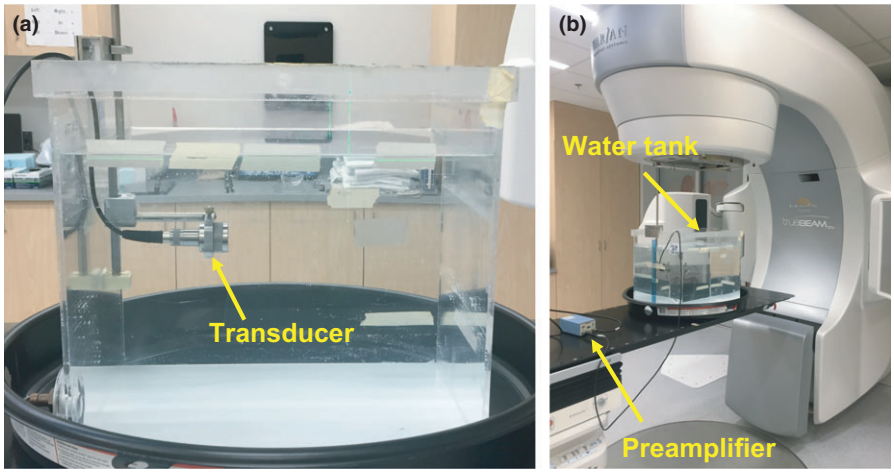

FIG. 2. Experimental set-up. (a) The immersion ultrasound transducer was positioned in the water tank at the depth of the imaging plane, perpendicular to the photon beam central axis. (b) The water tank sat on the patient couch, and the transducer output was fed into a commercial preamplifier. Not pictured here is the oscilloscope used to read out the signal, which was situated at the treatment console. [Color figure can be viewed at wileyonlinelibrary.com]

target pulse was used to trigger the oscilloscope, signals were sampled at a sampling frequency of 4 MHz, and 512 signals were averaged for each acquisition.

The acoustic signals induced in the water tank following the irradiation of fields of various shapes and sizes were investigated. Square and rectangular fields were defined by the primary collimator, and the multi-leaf collimator (MLC) was used to create non-standard fields. Note that all quoted field sizes were defined at an SSD of 100 cm rather than the depth of imaging. For imaging studies where transducer signals were acquired at multiple angles around the irradiated field, the transducer was kept in a stationary position while the collimator was rotated. Signals were acquired at 60 collimator positions, or every 6°. This step interval was chosen as a compromise between imaging speed and quality.

2.B. Simulation workflow

Simulated induced acoustic signals and XACT images were obtained using a previously developed and validated simulation workflow[13] combining radiotherapy EGSnrc Monte Carlo dose simulations[16,17] and the acoustic wave transport simulation toolbox k-Wave.[18] Simulated signals were convolved with the photon beam pulse shape shown in Fig. 1. A digital band-pass filter designed to match the frequency response of the experimental detection system was also applied to the simulated signals. Profiles extracted from simulated and experimental images were quantitatively compared using gamma analysis with a pass criteria of 3%/3 mm.[19]

2.C. Signal processing and image reconstruction

Prior to reconstruction, both simulated and experimental transducer signals were processed with a Savitzky-Golay denoising filter. A back projection algorithm was used to reconstruct images. Experimental images were inverted to account for the polarity change by the detection system, and all images were normalized such that the maximum pixel intensity was equal to one.

2.D. Extraction of dosimetric information from XACT images

XACT forms images of the initial differential pressure distribution following a single pulse of linac irradiation. The relationship between deposited heat energy, H, and induced differential pressure, p, at a given location, $\boldsymbol{r}$, is given by[6]

$$p(\boldsymbol{r}) = H(\boldsymbol{r}) \cdot \Gamma(\boldsymbol{r}) \tag{1}$$

where Γ is the Grüneisen coefficient, a material specific constant indicating the conversion efficiency between deposited heat energy and pressure. Note that Eq. (1) assumes that all heat energy from a single radiation pulse is deposited instantaneously. Rewriting Eq. (1) in terms of radiation dose, D, yields

$$p(\boldsymbol{r}) = D(\boldsymbol{r}) \cdot \rho(\boldsymbol{r}) \cdot (1 - k(\boldsymbol{r})) \cdot \Gamma(\boldsymbol{r}) \tag{2}$$

where ρ represents the physical density of the material at location $\boldsymbol{r}$, and k is the heat defect, which is the fraction of deposited energy that does not appear as heat. Since all images were acquired in a homogeneous water tank, the density, heat defect, and Grüneisen coefficients are constant over all pixels, and the reconstructed XACT images are therefore relative dose images.

2.E. Ion chamber and XACT profile comparison

To evaluate XACT as a potential dosimetry tool, dose profiles through the investigated fields were obtained with ion chamber (IC) measurements in a 3D water tank as per standard clinical QA protocols. The Blue Phantom[2] water tank dosimetry system and a CC13 ion chamber (IBA Dosimetry, Schwarzenbruck, Germany) were used. This ion chamber has an active volume of 0.13 cm^3, and volume averaging was not accounted for.

IC profiles and profiles extracted from experimental XACT images were quantitatively compared using gamma analysis.[19] A gamma criteria of 7%/4 mm was chosen based on the Radiology Physics Center complex dosimetry protocol recently used in a multi-center IMRT credentialing study.[20] The total gamma pass rate for a given profile was calculated for points in the jaw-defined field size region.

3. RESULTS

3.A. Acoustic signal characteristics

The simulated and experimental acoustic signals induced in a water tank following the irradiation of a 4 cm × 4 cm field at a depth of 10 cm are displayed in Fig. 3. At 10 cm depth, the jaw-defined field size is 4.4 cm × 4.4 cm. The spatial locations of the field and transducer are aligned with the time domain acoustic signals assuming that the speed of sound in water is 1480 m/s. A rarefaction trough and compression peak pair is observed in the signal at each boundary of the radiation field. At boundary one (B1) where the dose gradient is from low to high, as observed by the transducer, the rarefaction trough precedes the compression peak. The reverse is true at boundary two (B2) where the dose gradient is from high to low, and the compression peak precedes the rarefaction trough. The near edge of the field is 11.5 cm from the transducer, which corresponds to a time of 78 μs, while the far edge of the field is 15.9 cm from the transducer, corresponding to a time of 107 μs. These times coincide with the middle of the compression peak and rarefaction trough pair created at each field boundary.

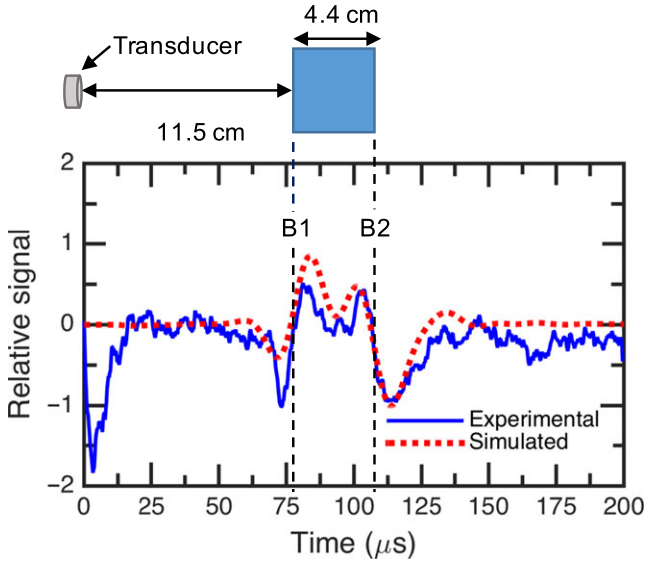

FIG. 3. The experimental and simulated transducer signals following the irradiation of a 4.4 cm × 4.4 cm field and the spatial locations of the radiation field and transducer assuming the speed of sound in water is 1480 m/s. At boundary one (B1) the dose gradient is from low dose to high dose and the rarefaction trough precedes the compression peak. The compression peak precedes the rarefaction trough at boundary two (B2) where the dose gradient is from high to low. The field edges occur at 78 μs and 107 μs, coinciding with the middle of each rarefaction trough and compression peak pair. [Color figure can be viewed at wileyonlinelibrary.com]

3.B. XACT image characteristics

The characteristics of XACT images were investigated experimentally and through simulations for a 4 cm × 4 cm field at depths of 2.4 cm and 10 cm. Figs. 4(a) and 4(b) display the experimental and simulated XACT images at a depth of 2.4 cm, while the images at a depth of 10 cm are shown in Figs. 5(a) and 5(b). The high-intensity square in the center of the images represents the primary radiation field. A negative intensity ring artifact surrounding the field is observed in both experimental and simulated images, and appears more continuous in the images at 10 cm compared to those at 2.4 cm. In the images at a depth of 2.4 cm, a large decrease in intensity is observed in the center of the radiation field.

3.C. Extracting dosimetric information from XACT images

To demonstrate the relationship between the intensity of XACT images and radiation dose, profiles were extracted from experimental and simulated XACT images and compared to IC measured profiles. Note that gamma test pass rates for all fields are summarized in Table I.

Figure 6 compares XACT and IC profiles for the 4 cm × 4 cm field at 10 cm depth. The corresponding XACT images were shown in Fig. 5. The agreement of profiles was quantified using gamma analysis in the jaw-defined field region from −2.2 cm to +2.2 cm. When the experimental XACT profile is compared to the IC measured profile, 77% of points pass a 7%/4 mm gamma test, with the largest deviations occurring in the center of the field. Comparing the simulated and experimental XACT profiles, 97% of points pass a 3%/3 mm gamma test.

Figure 7 displays the ability of XACT to image a 6 cm × 3 cm field at 10 cm depth. Figure 7(a) shows the experimental XACT image, while Fig. 7(b) displays the simulated XACT image. Figs. 7(c) and 7(d) compare the profiles extracted from the simulated and experimental XACT images in each dimension to IC measured profiles. Within the jaw-defined field size regions, 100% and 95% of experimental XACT profile points in the 3 cm and 6 cm dimensions, respectively, passed a 7%/4 mm gamma test when compared to ion chamber measurements. Comparing simulated and experimental XACT profiles, 94% and 89% of experimental XACT profile points pass a 3%/3 mm gamma test, in the 3 cm and 6 cm dimensions, respectively.

Figure 8 demonstrates the ability of XACT to reconstruct an off-centered field. Figs. 8(a) and 8(b) show the experimental and simulated XACT images, respectively, of a 4 cm × 4 cm field offset from center by 3 cm in both the negative X and Y directions. Figure 8(c) shows the profiles extracted from the experimental and simulated XACT images along the *x*-axis at Y = −30 mm, compared to the IC profile. In the jaw-defined field extending from −52 mm to −8 mm,

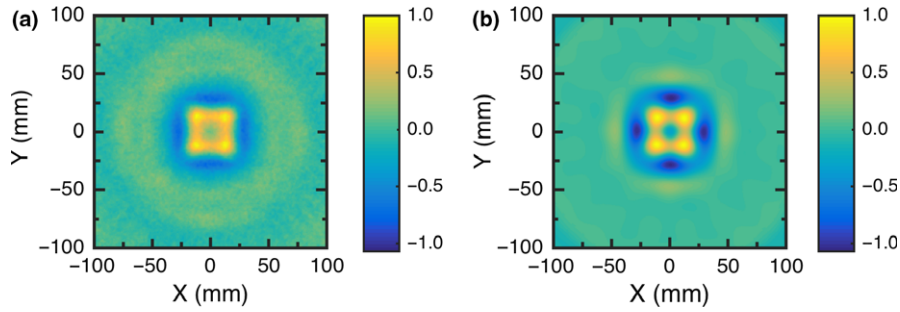

FIG. 4. (a) Experimental and (b) simulated XACT images of a 4 cm × 4 cm field at a depth of 2.4 cm. [Color figure can be viewed at wileyonlinelibrary.com]

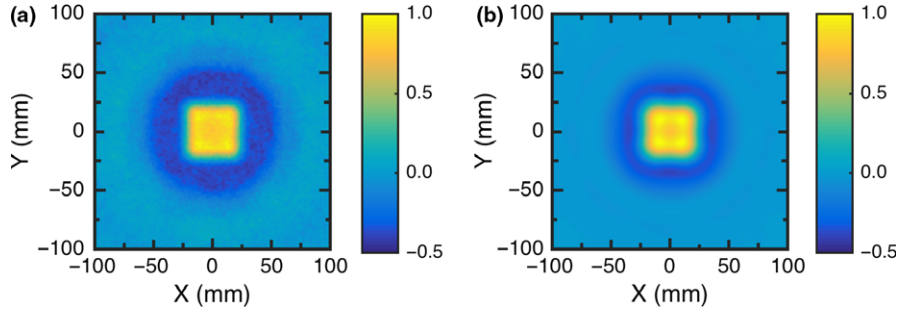

FIG. 5. (a) Experimental and (b) simulated XACT images of a 4 cm × 4 cm field at a depth of 10 cm. [Color figure can be viewed at wileyonlinelibrary.com]

TABLE I. Summary of gamma test pass rates for each investigated field considering the points in the jaw-defined field region.

Field	Profile location	Gamma test pass rate (7% / 4 mm) Ion chamber vs. experimental XACT	Gamma test pass rate (3% / 3 mm) Simulated vs. experimental XACT
4 cm × 4 cm (Fig. 5-6)	Y = 0 cm	77%	97%
6 cm × 3 cm (Fig. 7)	X = 0 cm (3 cm direction)	100%	94%
6 cm × 3 cm (Fig. 7)	Y = 0 (6 cm direction)	95%	89%
Off axis 4 cm × 4 cm (Fig. 8)	Y = −3 cm	79%	59%
Three rectangle (Fig. 9)	Y = 1 cm	63%	64%
2.5 mm gap (Fig. 10)	Y = 1 cm	77%	38%
Puzzle piece (Fig. 11)	Y = −1.5 cm	86%	80%

79% of experimental XACT points pass the 7%/4 mm gamma test when compared to IC measurements, and 59% of experimental points pass the 3%/3 mm gamma test when compared to the simulated XACT profile.

To test the ability of XACT to reconstruct complex fields, the MLCs were used to produce more complicated field shapes. Fig. 9 shows the investigation of a field pattern consisting of three 2 cm × 6 cm rectangles separated by 1 cm,

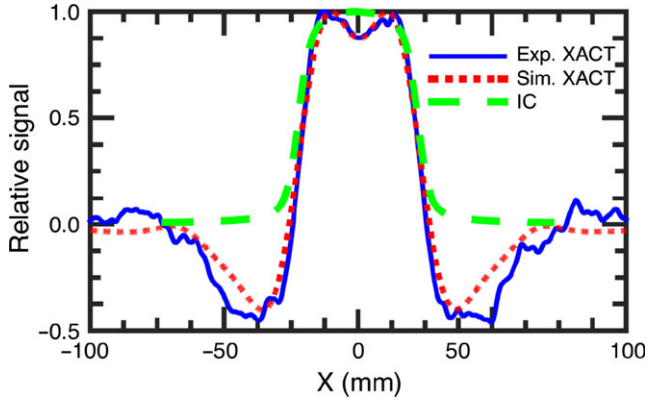

FIG. 6. Profiles extracted at Y = 0 mm from experimental and simulated XACT images of a 4 cm × 4 cm field at 10 cm depth compared to the IC measured profile. [Color figure can be viewed at wileyonlinelibrary.com]

as depicted by the block diagram in Fig. 9 (a). Figs. 9 (b) and (c) show the experimental and simulated XACT images, respectively, for this field at a depth of 10 cm, while Fig. 9(d) compares profiles extracted from the experimental and simulated XACT images at Y = 10 mm to the IC measured profile. In the jaw-defined region from −44 mm to +44 mm, 63% of experimental XACT profile points pass a 7%/4 mm gamma test when compared to IC measurements, while 64% of experimental XACT profile points pass a 3 %/3 mm gamma test when compared to the simulated XACT profile.

To explore the spatial resolution possibilities of XACT, Fig. 10 investigates a field consisting of a 3.25 cm × 6 cm rectangle and a 3 cm × 6 cm rectangle, separated by 2.5 mm, as depicted by the block diagram in Fig. 10 (a). Figs. 10(b) and 10(c) show the experimental and simulated

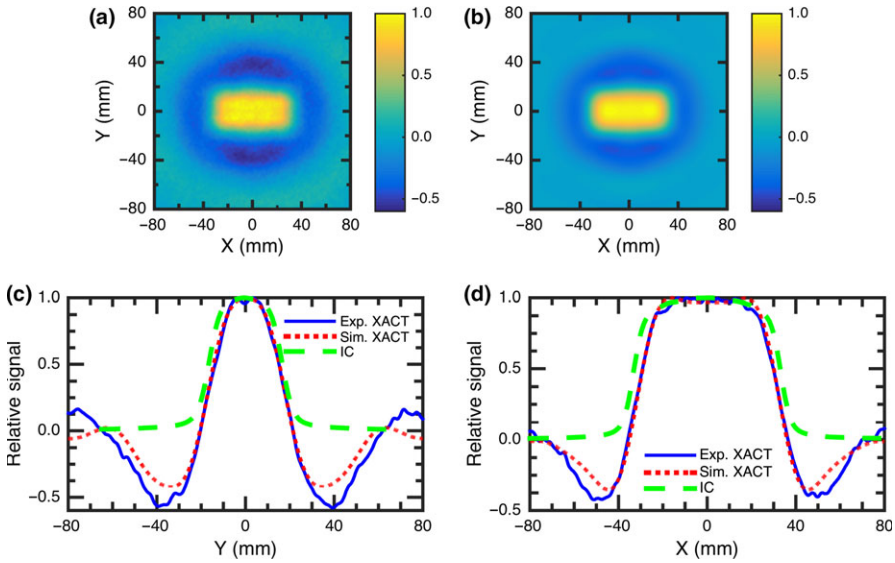

FIG. 7. (a) Experimental and (b) simulated XACT images of a 6 cm × 3 cm field at 10 cm depth. Comparison of profiles extracted from simulated and experimental XACT images and ion chamber measured profiles in the (c) 3 cm (X = 0) and (d) 6 cm (Y = 0) orientations. [Color figure can be viewed at wileyonlinelibrary.com]

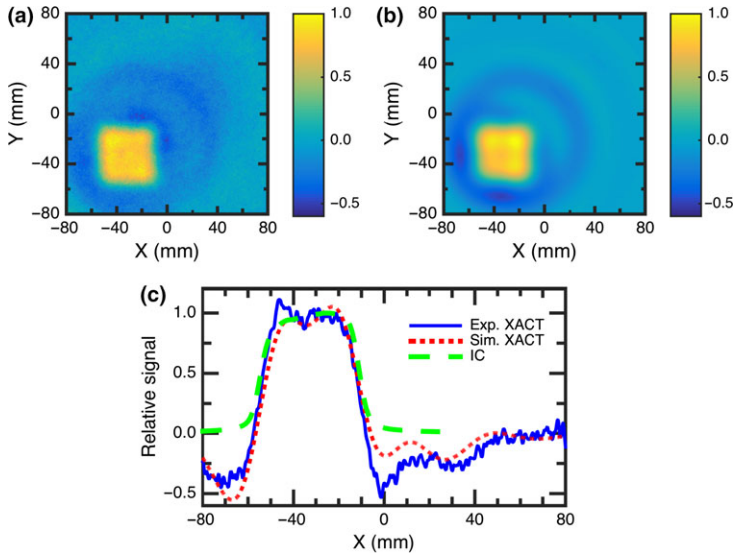

FIG. 8. (a) Experimental and (b) simulated XACT images of a 4 cm × 4 cm field centered at Y = −30 mm and X = −30 mm at a depth of 10 cm. (c) Comparison of profiles extracted from experimental and simulated XACT images and IC measurements along the *x*-axis at Y = −30 mm. [Color figure can be viewed at wileyonlinelibrary.com]

XACT images, respectively, of this field at a depth of 10 cm, while Fig. 10(d) compares profiles extracted from the simulated and experimental XACT images at Y = 10 mm to the IC measured profile. Seventy-seven percent of experimental XACT profile points between −35 mm and +35 mm pass a 7%/4 mm gamma test when compared to IC measurements, while 38% of the experimental XACT profile points pass a 3%/3 mm gamma test when compared to the simulated XACT profile.

Figure 11 demonstrates the ability of XACT to image a complex puzzle-piece shaped field, whose block diagram is shown in Fig. 11(a). The experimental XACT image at 10 cm depth is shown in Fig. 11(b), while Fig. 11(c) shows the simulated XACT image. Figure 11(d) shows a comparison between the profiles extracted from experimental and simulated XACT images at Y = −15 mm to the corresponding IC profile. Eighty-six percent of experimental XACT profile points between −35 mm and +35 mm pass a 7%/4 mm gamma test when compared to the IC profile, while 80% of experimental XACT profile points pass a 3%/3 mm gamma test when compared to the simulated XACT profile.

4. DISCUSSION

This work first investigated the properties of the induced acoustic signals in water following linac irradiation, as seen in Section 3.A. Figure 3 displays the acoustic signal from a

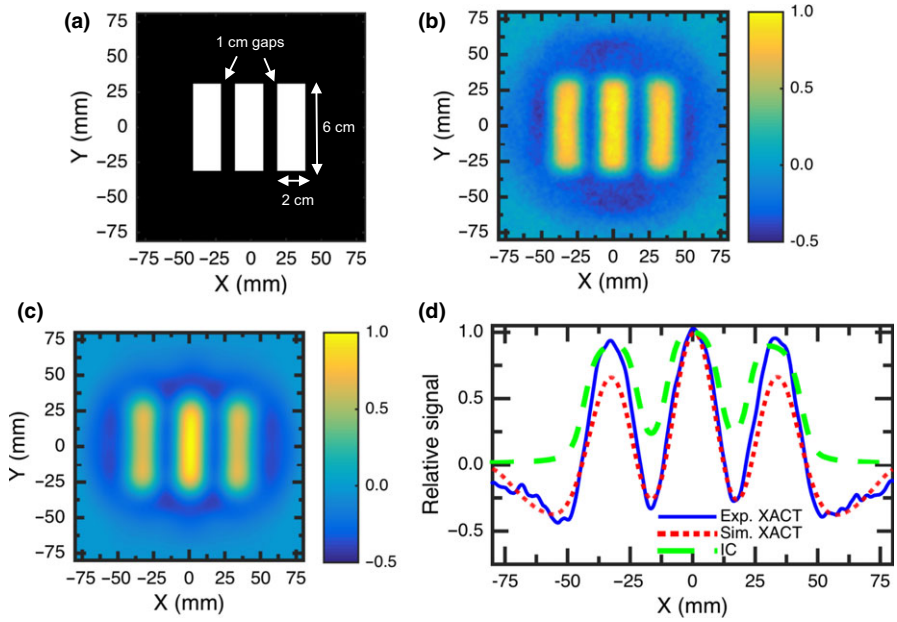

FIG. 9. (a) Block diagram showing the MLC positions projected to 100 cm SSD for a field pattern consisting of three 2 cm × 6 cm rectangles separated by 1 cm gaps, where the white regions represent the primary beam. (b) Experimental and (c) simulated XACT image of the field at 10 cm depth and (d) comparison of profiles extracted from the experimental and simulated XACT images and IC measurements along the *x*-axis at Y = 10 mm. [Color figure can be viewed at wileyonlinelibrary.com]

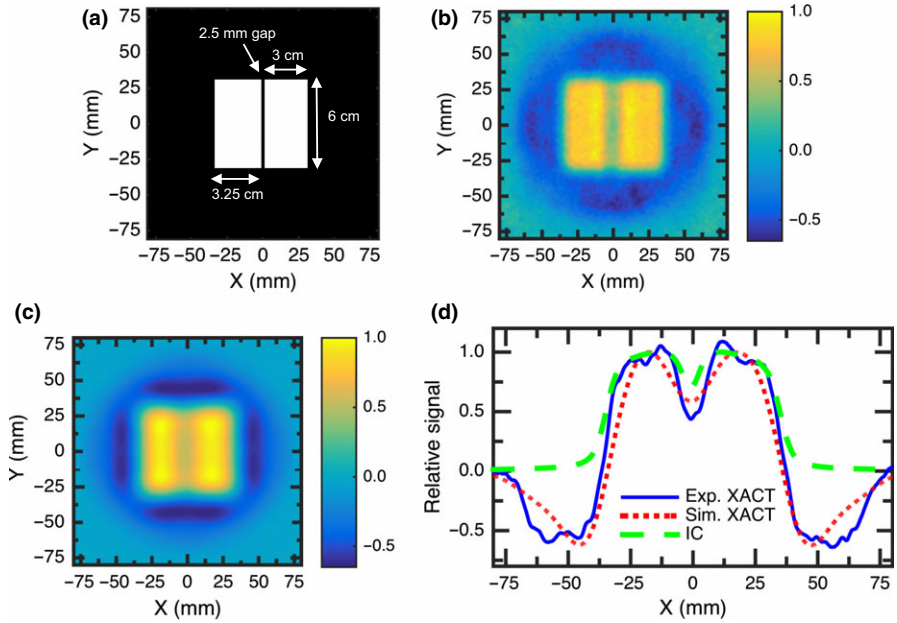

FIG. 10. (a) Block diagram showing the MLC produced field pattern at 100 cm SSD consisting of a 3.25 cm × 6 cm rectangle and a 3 cm × 6 cm rectangle separated by 2.5 mm. The white regions represent the primary beam. (b) Experimental and (c) simulated XACT images of the field at 10 cm depth. (d) Comparison of profiles extracted from experimental and simulated XACT images to IC measurements along the *x*-axis at Y = 10 mm. [Color figure can be viewed at wileyonlinelibrary.com]

4.4 cm × 4.4 cm field, and shows that a bipolar pulse is generated at each field edge. From photoacoustic theory, a single bipolar pulse is expected; however, due to the limited bandwidth of the transducer used in this work, the single bipolar pulse is split in two. This effect appears in the reconstructed XACT images as a decrease in signal intensity in the center of the field. This is especially noticeable in Fig. 4, where the imaging depth is 2.4 cm. In Fig. 5 at an imaging depth of 10 cm, out of plane acoustic signals help compensate for this effect. Thus, images acquired at 10 cm depth were used for comparison with IC measurements in section 3.C.

As seen in Table I, the agreement between profiles extracted from simulated and experimental XACT images is best for the simpler 4 cm × 4 cm and 6 cm × 3 cm fields. The larger discrepancies for the more complex MLC fields are partly due to the inclusion of profile points receiving a

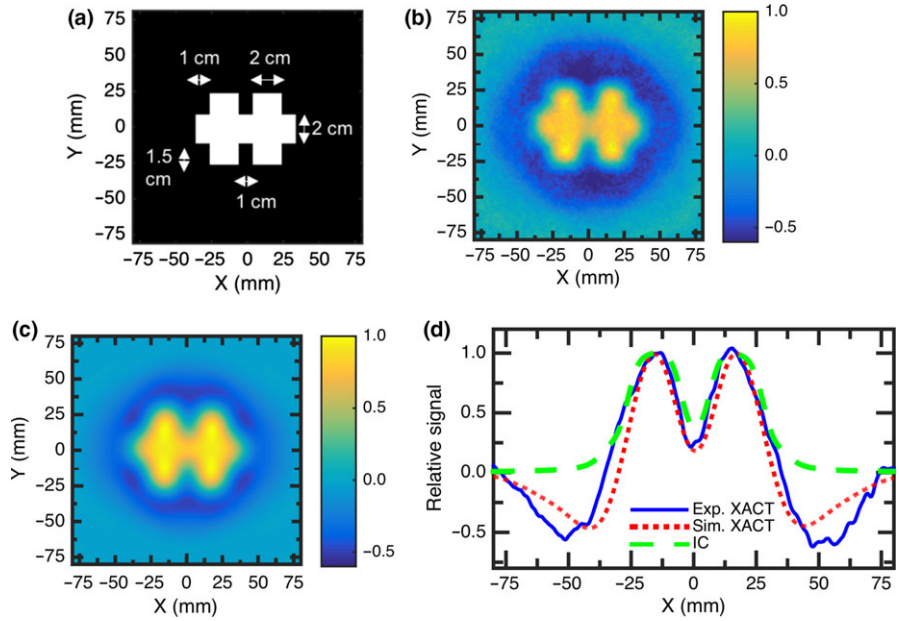

FIG. 11. (a) Block diagram showing the MLC produced field pattern at 100 cm SSD, where the white regions represent the primary beam. (b) Experimental and (c) simulated XACT images of the field at 10 cm depth. (d) Comparison of profiles extracted from experimental and simulated XACT images to IC measurements along the x-axis at Y = −15 mm. [Color figure can be viewed at wileyonlinelibrary.com]

low dose in the gamma analysis tests. In addition, uncertainty in the MLC Monte Carlo model likely contributed to this disagreement. It was observed that gamma test pass rates worsened in MLC fields with spatially close dose gradients, such as the 2.5 mm gap pattern, compared to patterns where the details were spatially farther apart, such as the puzzle-piece pattern. Both the experimental and simulated XACT images of the off axis 4 cm × 4 cm field appear distorted. This is likely due to the radiation field being spatially close to the transducer, which causes signal distortions due to the spatial characteristics of the ultrasound transducer and noise from the linac pulse. A striking feature of both the simulated and experimental XACT images is the existence of pixels with a negative intensity. As per Eq. (2), negative XACT values imply a negative dose, which has no physical meaning. While this work used a simple back projection reconstruction algorithm, a more advanced reconstruction algorithm, such as a model based inversion method that uses non-negative constraints,[21] could fix this problem.

The agreement of profiles extracted from XACT images with conventional ion chamber measured profiles indicates that XACT images have intensity related to the deposited dose. While a gamma criteria of 7%/4 mm is conservative and the pass rates presented in this paper may not be at clinically acceptable levels, these results are promising for a proof-of-principle study. This opens the possibility of using XACT as a dosimetry technique not only for relative water tank dosimetry, as shown in this work, but potentially also for *in vivo* dosimetry. In principle, XACT images could be formed during treatment by positioning ultrasound transducers around the patient.

In this study, XACT images were obtained by rotating the collimator and keeping the transducer in a stationary position. While this is possible for homogeneous or perfectly symmetrical objects, such as a water tank, this technique is time consuming and would not work for many cases. In addition, this implementation of XACT assumes a symmetric beam profile. Ideally, an array of transducers would surround the object or patient being imaged and the induced acoustic signals would be simultaneously measured by each transducer. Thus, an XACT image could be formed in a matter of seconds. With a transducer array, the images presented in this paper could be acquired at a dose of 0.56 Gy (1.11 mGy / pulse · 512 pulse averages) to the depth of maximum dose. It is possible that the number of signals averaged could be reduced, thus decreasing the dose.

It is important to emphasize that the induced acoustic signal strength depends on the localized temperature increase following a single pulse of linac irradiation, as per Eq. (1). Since the heat defect in water varies little over the relevant range of linear energy transfer (LET) values in photon radiotherapy,[22] beams of different energies depositing the same dose per pulse will cause a similar temperature increase, and will therefore induce acoustic signals of a similar strength. However, the dose per pulse is not constant across all energies on the linac used in this work. Images were acquired using a beam energy of 10 MV FFF because this gave the largest dose per pulse, and therefore the highest signal to noise ratio. Since the dose rate on the linac is varied by changing the pulse repetition frequency and the dose per pulse remains constant, XACT is dose rate independent.

There are numerous factors that could be optimized to improve agreement between experimental XACT and IC profiles. These include the number of transducer positions at which signals are obtained, signal processing and image reconstruction techniques, and transducer properties.

Implementing more advanced image reconstruction techniques is expected to be crucial for the success of XACT, especially *in vivo* where acoustic wave attenuation and scattering will affect the detected signals. In this case, acoustic properties could be extracted from a patient computed tomography (CT) or ultrasound scan[23] and used to guide and account for heterogeneities in image reconstruction.[24]

Figure 10 demonstrated the ability of XACT to resolve a 2.5 mm gap in the dose distribution. Ultimately, spatial resolution on the order of 0.5 mm–3 mm would be desirable for *in vivo* dosimetry, since stereotactic treatment is typically planned on CT scans with a slice thickness of 1 mm–3 mm.[25] To achieve this desired spatial resolution, appropriately designed transducers will be critical. The 0.5 MHz central frequency transducer used in this work limits spatial resolution in water to 3 mm. Increasing the transducer central frequency to 3 MHz would improve the achievable spatial resolution to 0.5 mm. While there is always a trade-off between ultrasound attenuation and resolution, the increase in ultrasound attenuation in water at a frequency of 3 MHz compared to 0.5 MHz is 0.018 dB/cm, and is therefore not a concern.[18] Another interesting factor that could be explored to improve spatial resolution is the width of the linac photon pulse. From photoacoustic theory, shorter pulses are expected to improve resolution since the energy is deposited in a shorter period of time.[6] In addition, assuming the integral energy delivered by the pulse is kept constant, decreasing the pulse width would also increase the amplitude of induced acoustic signals.

XACT has many advantageous characteristics that make its implementation as a radiotherapy dosimeter attractive. First, XACT is a real-time technique, meaning *in vivo* images could be obtained during treatment to ensure the delivered dose distribution is as expected. Also, provided that the transducers are placed outside of the beam path, XACT does not perturb the beam, eliminating the need for the perturbation correction factors required by many other dosimetry techniques. In addition, induced acoustic signals are linearly related to the amount of dose deposited, and are energy independent over photon energies of interest in radiotherapy. Using Eq. (2) to relate pressure to deposited dose, XACT could be used as an absolute dosimetry technique provided that the heat defect, physical density, and Grüneisen coefficient are accurately determined and the transducer and amplification system is well defined and calibrated.

While the term photoacoustic effect implies that a pulsed beam of photons is used to induce acoustic waves, a similar phenomenon has been observed with pulsed proton beams. Due to the importance of range verification in proton radiotherapy,[26] the acoustic waves induced following proton beam irradiation have been investigated experimentally and through simulations by a number of groups,[27–34] with the ultimate goal being to develop an *in vivo* technique capable of localizing the Bragg peak. While proton beams have different energy deposition mechanisms and beam profile characteristics than photon beams, the same principles from XACT apply since ultimately the induction of acoustic waves is dependent on heat energy deposition. Thus, the work presented here, in particular the imaging workflow, extraction of profiles from images, and signal processing/reconstruction techniques, could also be extended to imaging the dose distributions deposited by proton beams.

5. CONCLUSION

This work demonstrates that XACT images with intensity related to the amount of radiation dose deposited within a soft tissue mimicking object can be obtained for a variety of field sizes and shapes. Profiles extracted from XACT images were quantitatively compared to profiles obtained from ion chamber measurements. While this technique is still in its infancy and much work is required to optimize the detection of induced acoustic waves and the reconstruction of XACT images, this work indicates that XACT has potential in relative water tank and possibly *in vivo* dosimetry applications.

ACKNOWLEDGMENTS

The authors thank Dr. Stephen Davis and Mr. Kyle O'Grady for experimental assistance and linac beam models. S. H. acknowledges support by the NSERC CREATE Medical Physics Research Training Network grant 432290. This work is partly supported by the Canadian Institutes of Health Research (CIHR) grants MOP-114910 and MOP-136774 and the University of Michigan Cancer Center fund G017459.

CONFLICTS OF INTEREST

The authors have no relevant conflicts of interest to disclose.

[a)]Author to whom correspondence should be addressed. Electronic mail: susannah.hickling@mail.mcgill.ca; Telephone: +1 (514) 934 1934 ext. 48114.

REFERENCES

1. Attix FH. *Introduction to Radiological Physics and Radiation Dosimetry*. New York: Wiley- VCH; 2004.
2. Podgorsak EB. *Radiation Oncology Physics: A Handbook for Teachers and Students*. Vienna: International Atomic Energy Agency; 2005.
3. IAEA. Development of procedures for in vivo dosimetry in radiotherapy. *IAEA Hum Heal Reports*. 2013;8:40.
4. Mijnheer B, Beddar S, Izewska J, Reft C. In vivo dosimetry in external beam radiotherapy. *Med Phys*. 2013;40:070903.
5. Bell AG. On the production and reproduction of sound by light. *Am J Sci*. 1880;20:305–324.
6. Wang L, ed. *Photoacoustic Imaging and Spectroscopy*. Boca Raton: CRC Press Taylor Francis Group; 2009.
7. Wang L, Hu S. Photoacoustic tomography. In vivo Imaging from organelles to organs. *Science*. 2012;335:1458–1462.
8. Yao J, Wang L. Photoacoustic tomography: fundamentals, advances and propspects. *Contrast Media Mol Imaging*. 2011;6:332–345.
9. Sachse W. Observation of X-Ray generated ultrasound. In: *IEEE Ultrason. Symp. Proc*. 1983: 677–680.

10. Bowen T, Chen CX, Liew SC, Lutz WR, Nasoni RL. Observation of ultrasonic emission from edges of therapeutic x-ray beams. *Phys Med Biol*. 1991;36:537–539.
11. Xiang L, Han B, Carpenter C, Pratx G, Kuang Y, Xing L. X-ray acoustic computed tomography with pulsed x-ray beam from a medical linear accelerator. *Med Phys*. 2013;40:010701.
12. Xiang L, Tang S, Ahmad M, Xing L. High Resolution X-ray-Induced Acoustic Tomography. *Sci Rep*. 2016;6:26118.
13. Hickling S, Leger P, El Naqa I. On the detectability of acoustic waves induced following irradiation by a radiotherapy linear accelerator. *IEEE Trans Ultrason Ferroelectr Freq Control*. 2016;63:683–690.
14. Diao X, Zhu J, Li W et al. Broadband detection of dynamic acoustic emission process induced by 6 MV therapeutic X-ray beam from a clinical linear accelerator. In: *IEEE Int. Ultrason. Symp. Proc*. 2015:1–4.
15. Sampaio DRT, Uliana JH, Antonio AO, Pavoni JF, Pavan TZ. X-ray acoustic imaging for external beam radiation therapy dosimetry using a commercial ultrasound scanner. In: *IEEE Int. Ultrason. Symp. Proc*. 2015: 1–4.
16. Rogers DWO, Faddegon BA, Ding GX, Ma CM, We J, Mackie TR. BEAM: a Monte Carlo code to simulate radiotherapy treatment units. *Med Phys*. 1995;22:503.
17. Walters B, Kawrakow I, Rogers DWO. *DOSXYZnrc Users Manual*. Ottawa: NRC Canada; 2011.
18. Treeby BE, Cox BT. k-Wave: MATLAB toolbox for the simulation and reconstruction of photoacoustic wave fields. *J Biomed Opt*. 2010;15:021314.
19. Low D, Harms W, Mutic S, Purdy J. A technique for the quantitative evaluation of dose distributions. *Med Phys*. 1998;25:656–661.
20. Weber DC, Vallet V, Molineu A et al. IMRT credentialing for prospective trials using institutional virtual phantoms: results of a joint European Organization for the research and treatment of cancer and radiological physics center project. *Radiat Oncol*. 2014;9:123.
21. Ding L, Deán-Ben X.L, Lutzweiler C, Razansky D, Ntziachristos V. Image reconstruction in cross-sectional optoacoustic tomography based on non-negative constrained model-based inversion. In: *Proc. SPIE*. 2015: 953919–953924.
22. Ross CK, Klassen NV. Water calorimetry for radiation dosimetry. *Phys Med Biol*. 1996;41:1–29.
23. Mast TD. Empirical relationships between acoustic parameters in human soft tissues. *Acoust Res Lett online*. 2000;1:37–42.
24. Treeby BE, Zhang EZ, Cox BT. Photoacoustic tomography in absorbing acoustic media using time reversal. *Inverse Probl*. 2010; 26:115003.
25. Benedict SH, Yenice KM, Followill D et al. Stereotactic body radiation therapy: the report of AAPM Task Group 101. *Med Phys*. 2010; 37:4078.
26. Knopf A-C, Lomax A. In vivo proton range verification: a review. *Phys Med Biol*. 2013;58:R131–R160.
27. Hayakawa Y, Ph D, Tada J, Arai N. Acoustic pulse generated in a patient during treatment by pulsed proton radiation beam. *Radiat Oncol Investig*. 1995;3:42–45.
28. Jones KC, Witztum A, Sehgal CM, Avery S. Proton beam characterization by proton-induced acoustic emission: simulation studies. *Phys Med Biol*. 2014;59:6549–6563.
29. Assmann W, Kellnberger S, Reinhardt S, et al. Ionoacoustic characterization of the proton Bragg peak with submillimeter accuracy. *Med Phys*. 2015;42:567–574.
30. Parodi K, Assmann W. Ionoacoustics: a new direct method for range verification. *Mod Phys Lett A*. 2015;30:1540025.
31. Ahmad M, Xiang L, Yousefi S, Xing L. Detection threshold of proton-acoustic range verification. *Med Phys*. 2015;42:5735–5744.
32. Jones KC, Vander Stappen F, Bawiec C et al. Experimental observation of acoustic emissions generated by a pulsed proton beam from a hospital-based clinical cyclotron experimental observation of acoustic emissions generated by a pulsed proton beam from a hospital-based clinical cyclotron. *Med Phys*. 2015;42:7090–7097.
33. Alsanea F, Moskvin V, Stantz KM. Feasibility of RACT for 3D dose measurement and range verification in a water phantom. *Med Phys*. 2015;42:937.
34. Jones KC, Seghal CM, Avery S. How proton pulse characteristics influence protoacoustic determination of proton- beam range: simulation studies. *Phys Med Biol*. 2016;61:2213–2242.